An MRI Investigation of Trickle Flow

Ali Fathiganjehlou[a], K.A. Buist[a], E.A.J.F. Peters[a,*], A.H.J de Graaf[a], J.A.M. Kuipers[a]

[a]*Multiphase Reactors Group, Department of Chemical Engineering and Chemistry, Eindhoven University of Technology, Eindhoven, 5600 MB, The Netherlands*

Abstract

Trickle bed reactors (TBR) are widely used in the chemical industries. These reactors involve gas and liquid flow through a catalyst-packed bed. For optimal TBR performance, it is crucial to achieve a uniform distribution of gas and liquid among the catalyst particles. However, in multi-tubular reactors with slender tubes, flow maldistribution near the tube walls is a common issue. Therefore, a comprehensive understanding of local phase and flow distribution is essential for designing and operating reactors with slender tubes. This study employs Magnetic Resonance Imaging (MRI) to characterize the three-dimensional distribution of the two-phase trickle flow within a slender tube. Three quantities are characterized: gas-liquid-solid distribution, particle wetting efficiency, and the flow field. Structure and flow MRI images are processed to calculate these quantities. Additionally, a novel post-processing technique is introduced to determine the liquid distribution over individual particle surfaces. This distribution is determined at several axial and radial positions.

Keywords: Magnetic Resonance Imaging, Flow imaging, Two-phase hydrodynamics, Wetting efficiency, Saturation,

1. Introduction

A Trickle Bed Reactor (TBR) is a chemical reactor type with important applications in various chemical and petrochemical processes, such as: hydrogenation, hydro-processing, and oxidation. A TBR accommodates a fixed packing of catalytic particles with a co-current downward two-phase gas-liquid flow. The packing enables the distribution of the liquid and gas inside the TBR and provides a large internal surface area for the heterogeneous catalytic reactions. The quality of the gas-liquid distribution and the gas-liquid-solid contact throughout the bed plays a vital role in the performance of TBR.

---

*Corresponding author. Tel: +31-402473122 E-mail address: e.a.j.f.peters@tue.nl (E.A.J.F. Peters).

A uniform distribution of the flows ensures that all the particles in the bed are exposed to the same conditions and that the reaction takes place at a uniform rate throughout the bed. However, when the flows are not distributed evenly, some parts of the bed are exposed to higher or lower concentrations of reactants. This can result in hot spots or cold spots, where the reaction rate is higher or lower than it should be. This can cause an overall reduction in reactor performance, and may even lead to thermal runaway in case of highly exothermic chemical reactions.

The distribution of liquid can be characterized by different parameters. For the liquid phase, the so-called saturation is defined as the fraction of the void space occupied by liquid, and its distribution has a direct impact on the particle wetting and pressure drop of the TBR. The other parameter is particle wetting, which is defined as the fraction of a catalytic particle's external surface that is covered with liquid. The wetting of catalyst particles has a direct impact on their efficiency within the reactor. Both the average wetting efficiency and the distribution of particle wetting are critical parameters that greatly influence the reactor performance [1]. Depending on which phase contains the limiting reactant, an increase in the particle wetting can be either favorable or unfavorable for the degree of chemical conversion. If the limiting reactant is in the gas phase, low particle wetting is desired, as there is a higher direct contact area of the gas phase with the catalytic particle. On the other hand, if the limiting reactant is in the liquid phase, complete particle wetting is desired. In this case, the higher the extent of particle wetting, the higher the contact area between the liquid and catalytic particles, and the higher the conversion rate will be [2].

Apart from the phase distribution, the local velocity and flow distribution affect TBR performance. Liquid preferentially flows through paths with a lower hydraulic resistance, and this causes a maldistribution in terms of local liquid flow rates. In the areas with stagnant and low liquid velocities, the local residence time is higher and the active sites of the particles' surface become saturated and less efficient. Additionally, the chance of the hot-spot formation increases because the flow of liquid is not efficiently removing the generated heat of the reaction. On the other hand, in the case of high local liquid velocities, the larger residence time distribution (RTD) causes a lower conversion. [3, 4]

A multi-tubular configuration is often used for TBR systems with large heat effects. In this design, the slender tubes filled with catalytic particles have a typical tube-to-particle diameter ranging from 3 to 10. In a slender tube, the flow maldistribution is more noticeable because of intensified wall effects. Therefore, a detailed understanding of the two-phase hydrodynamics and liquid distribution in slender tubes is crucial in designing and optimizing a multi-tubular TBR and avoiding issues such as high pressure drop and thermal runaway.

Thus far, various numerical and experimental approaches have been employed to investigate the two-phase hydrodynamics inside a trickle bed. Particle-resolved Computational Fluid Dynamics (CFD) methods, such as the Volume of Fluid (VOF) method [5, 6, 7, 8, 9, 10] and Euler-Euler methods [11, 12, 13], are a couple of popular numerical approaches to model and investigate trickle beds [14]. An appropriate experimental technique that can provide local infor-

mation on the two-phase flow texture and hydrodynamics inside a trickle bed can greatly help validate and develop such computational models.

Various experimental approaches [15, 16] such as tracer injection methods [17], liquid collection at the bottom of the reactor [18, 19, 20, 21, 22, 23], dye adsorption [24, 25], heater probe [26], conductance probe [27], optical fiber probe [5], conductivity probe techniques [28] and advanced imaging techniques such as computer-assisted tomography [29], γ-ray tomography [30, 31], and capacitance tomography [32, 33] have been employed to investigate the two-phase flow structure inside a trickle bed. Most of the mentioned experimental approaches are practical only for measuring the macroscopic hydrodynamic characteristics of a trickle bed, such as the overall liquid hold-up and pressure drop, due to particular technical limitations of the experimental method. One of the exciting experimental approaches that enables local investigations of the microscopic two-phase hydrodynamics in fine spatial resolutions in three dimensions inside a trickle bed is Magnetic Resonance Imaging (MRI).

MRI is a promising technique in the non-invasive investigation of complex single-phase and two-phase flow structures and hydrodynamics in optically-opaque systems. MRI employs the spin properties of atom nuclei to create 3D images of a flow. One nucleus with proper spin properties that can be visualized using MRI is the Hydrogen nucleus.

MRI imaging of a two-phase flow inside a trickle bed can provide both the 3D flow structure, and the 3D local hydrodynamic properties of the flow, such as the local velocity distribution. MRI allows the visualization of the gas-liquid-solid contact points with fine resolutions, enabling measurement of the local wetting efficiency and saturation fields in a trickle bed. Moreover, MRI flow imaging enables investigation of the local hydrodynamics to characterize non-ideal flow behaviors, such as flow maldistribution.

Thus far, various research has been conducted to investigate and understand the detailed two-phase hydrodynamics of the flow inside a trickle bed using MRI [34, 35]. MRI has been employed to investigate the effects of gas and liquid flow rates on liquid hold-up, wetting efficiency, pore filling, and rivulet formation [36, 37, 38], as well as measurement of the local liquid and gas velocity field [39, 40, 41]. Furthermore, MRI has been used to investigate the two-phase hydrodynamics in different regimes, such as pulsing and trickling regimes, and the transition between them. [42, 43]

This work utilizes MRI to investigate the spatial distribution of two-phase flow parameters in a slender trickle bed, including liquid saturation, particle wetting, and liquid velocity and flow distribution. The objective is to characterize the impact of wall effects, which are commonly observed in slender packed columns, on the aforementioned parameters. To achieve this, axial and radial liquid saturation profiles are determined at different liquid flow rates to examine the 3D distribution. These profiles illustrate how the liquid spreads within a slender trickle bed across both the cross-section and length of the column.

Additionally, a novel method has been developed to calculate the local surface wetting of each spherical particle in the trickle column. The local surface wetting distribution of each particle is determined by dividing the particle sur-

3

face into numerous surface fragments and classifying each fragment as either wet or non-wet. The obtained local particle wetting profiles are utilized to characterize the 3D particle wetting distribution throughout the column. Finally, the radial velocity and flow profiles are plotted to analyze flow maldistribution.

In the following paragraphs, first, the experimental setup used for MRI structure and flow imaging is described. Then, the post-processing of the obtained images to calculate the distribution parameters, such as saturation field, particle wetting, and flow field is explained. Finally, in the results and discussion section, the calculated parameters used for characterizing the 3D liquid distribution, particle wetting, and flow inside a slender trickle bed are described.

2. Material and Methods

The experimental setup used for performing the MRI imaging of the trickle bed is shown in Figure 1. N_2 gas at 1 bar is used as the gas phase, and deionised water doped with 3 mM gadopentetic acid (Merck, 97%, anhydrous) and saturated with Nitrogen is used as the liquid phase in the trickle bed column. A cylindrical column of polycarbonate ($D = 21$ mm, $L = 61$ mm) filled with 3 ± 0.05 mm mono-disperse polypropylene spheres has been used for the trickle bed. The liquid flow is pumped into the column from above on top of the packing particles using a peristaltic pump (Watson-Marlow Qdos60 Universal) with a dampener to avoid pulsating flow in the entrance. An ultrasonic flow meter (Cori-Flow M15-AAD-55-0-S, Bronkhorst®) is used to read the liquid flow rate, and a rotameter is used for monitoring the gas flow rate. In order to have a proper distribution of the gas flow in the inlet, a porous glass frit with 90 μm pore size and 6 mm thickness is used on top of the packing. A hole with a diameter of 2 mm in the center of the glass frit is used to introduce the liquid (single-point liquid inlet). A detailed schematic of the top cap for the gas and liquid flows is shown in Figure 2.

A 7 Tesla cryogen-free MRI machine (MR SOLUTIONS, Guildford, UK) is used for imaging purposes. The packed column is positioned inside a plastic holder and inserted inside the bore of the vertical MRI scanner. A 1H quadrature transceiver coil with an inner diameter of 35 mm is used for imaging the Hydrogen protons inside the trickle column. For structure imaging, a 3D Fast Low-Angle Shot (3D FLASH) sequence (TE: 0 ms, TR: 20 ms, FA: 20 deg, FOV: $25.6 \times 25.6 \times 51.2$ mm^3, MTX: $128 \times 128 \times 256$, RES: $0.2 \times 0.2 \times 0.2$ mm^3, NA: 1, NR: 1), and for flow imaging, a Phase-Contrast Gradient Echo (PCGRE) sequence (TE: 3 ms, TR: 100 ms, FA: 15 deg, FOV: $25.6 \times 25.6 \times 51.2$ mm^3, MTX: $128 \times 128 \times 256$, RES: $0.2 \times 0.2 \times 0.2$ mm^3, NA: 1, NR: 1) is used. The implementation of the sequences is provided by the Preclinical Scan software (MR SOLUTIONS, Guildford, UK).

Both the FLASH3D and PCGRE images are taken from a section of the column with length 51.2 mm. Slices within a 12.8 mm distance from either ends of the section are excluded from the analysis due to the possibility of wrap-around artifacts in those slices. The time required for the FLASH3D imaging is 10.9 minutes (2.55 seconds per slice), and for the PCGRE imaging is
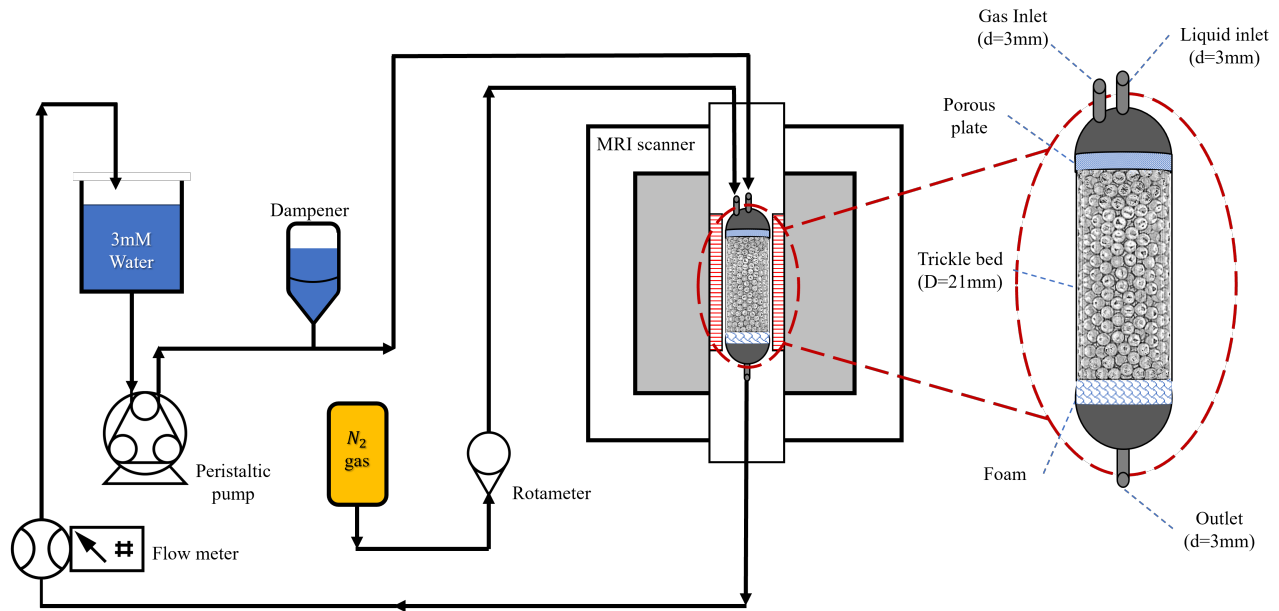
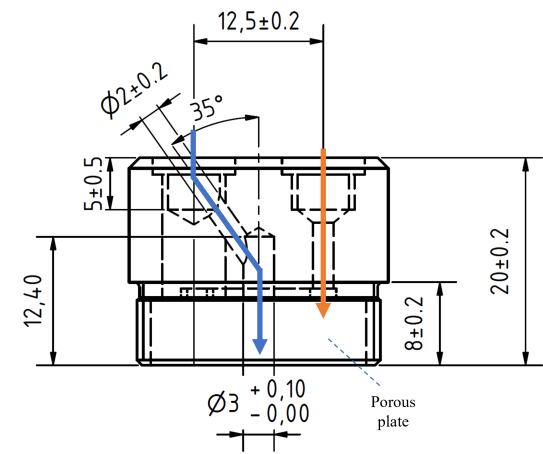Figure 1: The experimental setup for MRI imaging of the trickle bed.

Figure 2: A schematic of the top cap. The orange and blue lines show the gas and liquid flow entrances, respectively.

<div align="center">(a)   (b)</div>
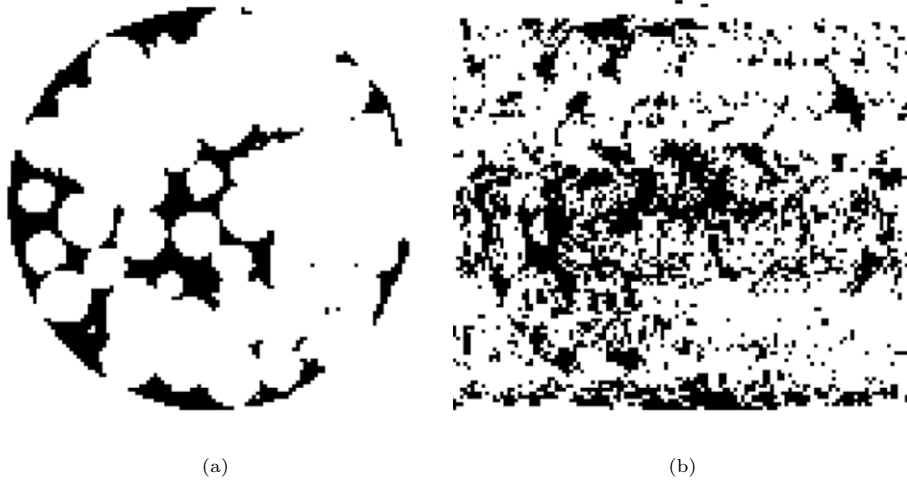
Figure 3: Structure images from a two-phase flow: the liquid hold-up in a cross-sectional slice of the column (a), and the same slice but the liquid voxels are smeared because of the motion artifact (b). The dark voxels represent the liquid phase.

109.3 minutes (25.61 seconds per slice). Motion artifacts are caused by unstable motion of the liquid phase while imaging and cause smearing in k-space[44]. To avoid these artifacts, MRI images are acquired after waiting a few minutes to allow the two-phase flow to stabilize. Figure 3 compares the same slice without and with motion artifacts.

2.1. Structure images

In the structure images obtained with the FLASH sequence, the voxels (volume elements) with higher intensities represent the liquid phase. The obtained structure images are binarized; voxels with a value of one are assigned to the liquid, and the voxels with a value of zero are assigned to the non-liquid phases (solid and gas). To obtain the structure images, first the column is flooded with the liquid flow for a couple of hours to ensure that there are no bubbles left in the column and all the void space is filled with liquid. Then, the MRI imaging is performed that results in structure images from the single-phase flow. To obtain the images from the two-phase flow, the gas flow is introduced into the column. After waiting for a couple of minutes for the flow to stabilize, the imaging is performed.

The 3D structure image from single-phase liquid flow provides the void space that is fully filled with liquid. The 3D structure image from the two-phase flow shows the liquid distribution inside the column. By subtracting these two images, it is possible to distinguish between the gas, liquid, and solid phases, i.e., the phase distribution map, which is needed to determine other relevant parameters. In this section, the methodology for post-processing of the MRI images to obtain the saturation profiles and particle wetting efficiencies is described. First,
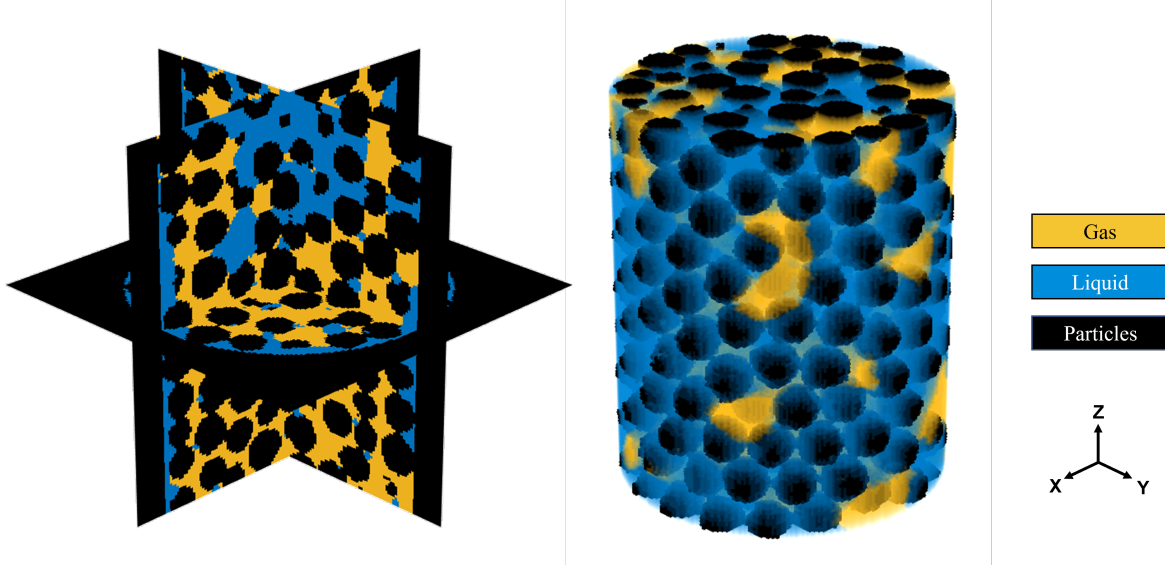
Figure 4: 3D phase distribution map of a two-phase flow inside a trickle column. The yellow, blue, and black volumes represents the gas, liquid, and solid phases, respectively.

the methodology used for calculating the saturation fields is discussed. Next, the steps for measuring the particles local wetting area is explained. For performing the post-processing steps, ImageJ v1.53e [45] and MATLAB v9.6 [46] software is employed.

2.1.1. Saturation field calculations

For calculating the liquid saturation, first, the obtained structure images from both single-phase and two-phase flows are binarized using the default binarization method of ImageJ. This binarization method is based on defining a threshold by analyzing the histogram of the images [45]. After the binarization, the single-phase and two-phase image sequences are saved in a 3D image volume format, i.e., RAW, and imported on a MATLAB script [47] for the subsequent post-processing. The combination of the 3D structure images from the single-phase and two-phase flows produces the 3D phase distribution map (Figure 4). From this map, it is possible to determine the distribution of the gas, liquid, and solid phases, i.e., the saturation profiles. The axial saturation profile along the column is calculated by summing the number of liquid voxels at each cross-sectional slice, perpendicular to the flow direction, in the two-phase image and dividing it by the one from the single-phase image.

For calculating the radial saturation profiles, the single-phase and two-phase images are binned in the radial direction. It was noticed that there is a slight geometrical distortion in the MRI images, which could be because of the imbalance of the spatial encoding gradients, making it difficult to calculate a correct radial profile. This geometric distortion in the single-phase 3D image is corrected
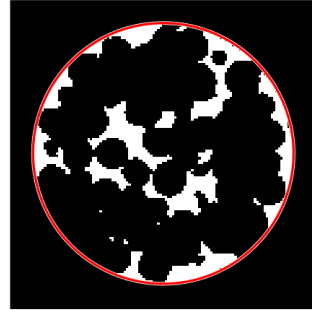
7
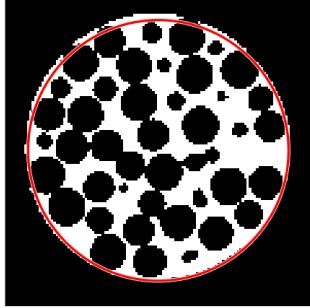
(a) Single-phase (before correction)
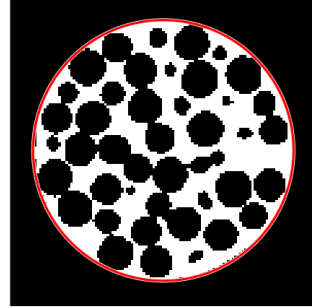
(b) Single-phase (after correction)
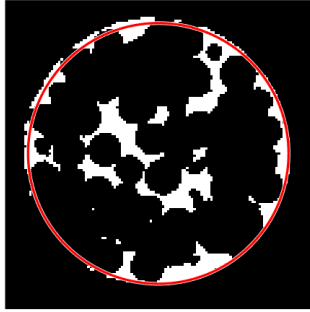
(c) Two-phase (before correction)

(d) Two-phase (after correction)

Figure 5: The single-phase and two-phase images before (a, c) and after (b, d) geometrical correction. In these cross-sectional slices, the white voxels represent the liquid phase.

using a linear interpolation method. The needed correction is determined from the distortion of the single-phase MRI images and applied to correct the two-phase images. After the correction, the radial saturation profile is calculated. Figure 4 shows an example of the single-phase and two-phase images before and after geometrical correction.

2.1.2. Wetting perimeter calculations

From the corrected images, it is also possible to calculate the wetting perimeters. The perimeter of the particle wetted by liquid in each slice is measured by: first, calculating the outline of the particles in the single-phase image, and then multiplying it to the liquid outline from the two-phase image. The outline is calculated using the *bwperim* function of Matlab. In order to avoid any mismatches between the particles outline from the single-phase image and the one from the two-phase image, the particle outline from the single-phase image is dilated by one voxel in each direction using the *imdilate* function of Matlab.

(a) Particles outline

(b) Thickened
Particles outline

(c) Liquid outline in a
two-phase flow

(d) Particles wetted
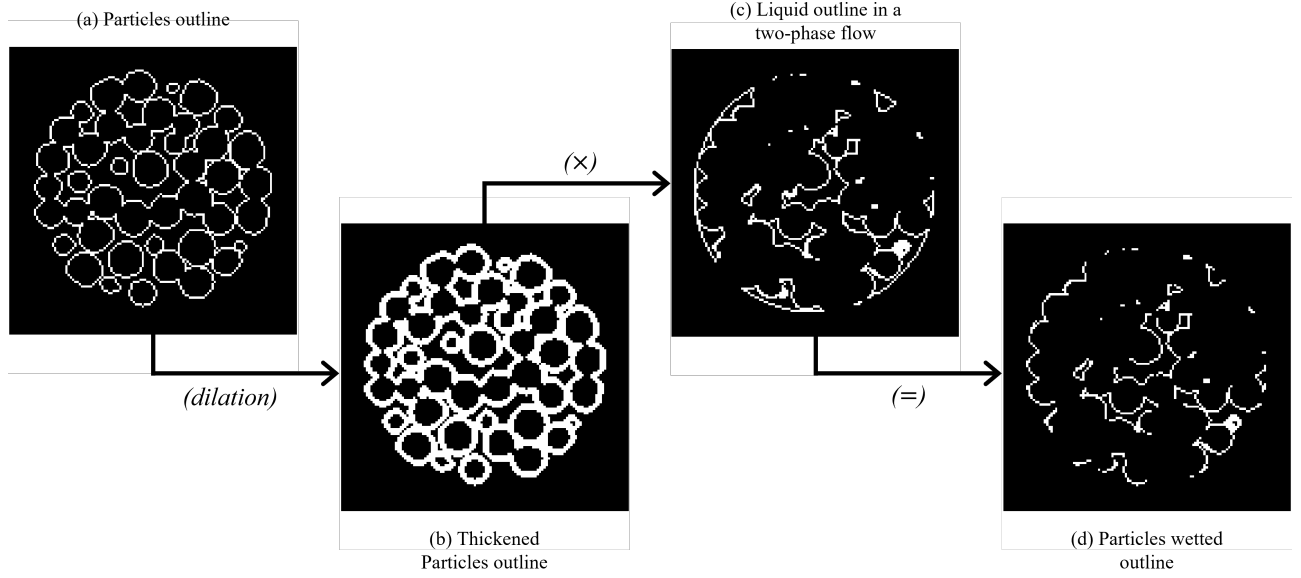outline

(dilation)

(×)

(=)

Figure 6: A schematic representation of the steps for particle wet perimeter calculation. In these cross-sectional slices, the white voxels represent the liquid phase.

Figure 6 shows a schematic representation of the particle wet perimeter calculation. The particle wet-perimeter fraction is calculated by counting the number of liquid voxels in Figure 6(d) and dividing it to the number of liquid voxels from Figure 6(a).

2.1.3. Particle wetting area calculations

To calculate the wet area of each particle, the particles first need to be detected from the single-phase image and reconstructed. For detecting the particles, the MRI images are binarized using the Renyi Entropy binarization algorithm [48] of ImageJ as a higher number of liquid voxels on the edges is conserved with this binarization scheme. With Renyi Entropy binarization method, it was observed that certain noises, such as those within particles, were not effectively eliminated. This presents a challenge in the calculation of the saturation field, however, it is a relatively minor concern in the calculation of particle wetting. This is because, in the latter calculation, only liquid voxels in contact with the particle are relevant. The single-phase and two-phase binarized images are geometrically corrected using the linear interpolation method as discussed earlier. Then, the corrected single-phase image is processed using a 3D Distance Transform Watershed algorithm of MorphoLibJ plugin of ImageJ to separate the touching particles [49]. Afterwards, a Hough transform [50] is performed on the 3D processed single-phase structure image, and the centers of particles are detected. Using the information regarding the particle centers, the particle packing is reconstructed. Figure 7 shows an schematic of the reconstructed bed.
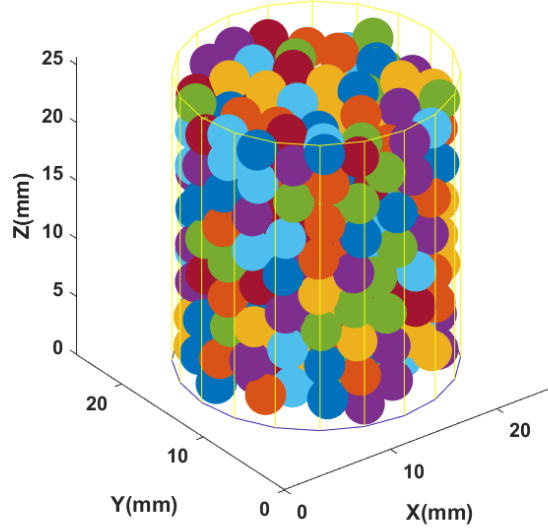
Figure 7: A 3D representation of the reconstructed packed bed.

The surface of the reconstructed particles is sliced into thousands of fragments. To cut the sphere surface in fragments, first, the particle is sliced in the z direction. Consider a sphere sliced up in n_z slices of equal thicknesses Δz $(= 2R/n_z)$. Each of these slices has the same surface area, namely, $2\pi R\Delta z$. Next, each slice is divided into n_{angles} pie parts in the angular direction. The area of each surface fragment is:

$$A^{frag.} = 2\pi R\Delta z/n_{angles} \qquad (1)$$

A schematic representation of the particle surface slicing is shown in Figure 8. In this work, each sphere surface is divided into 50 segments in both z and angular directions, resulting in a total number of 2500 surface fragments on each particle. The center of each surface fragment is localized in a voxel in the 3D two-phase structure image. If the corresponding voxel is in the liquid state, the area of that fragment is considered as a wet area fragment. The sum of wet area fragments divided by the total particle surface area defines the wet-area fraction of that particle. It is important to note that both the single-phase and two-phase images are dilated one voxel to reduce the inaccuracies induced by misplacement of the particles.

2.2. Flow images

The flow images are taken from the single-phase and two-phase flows using the PCGRE scan to visualize the local liquid velocity field. Firstly, the column

10

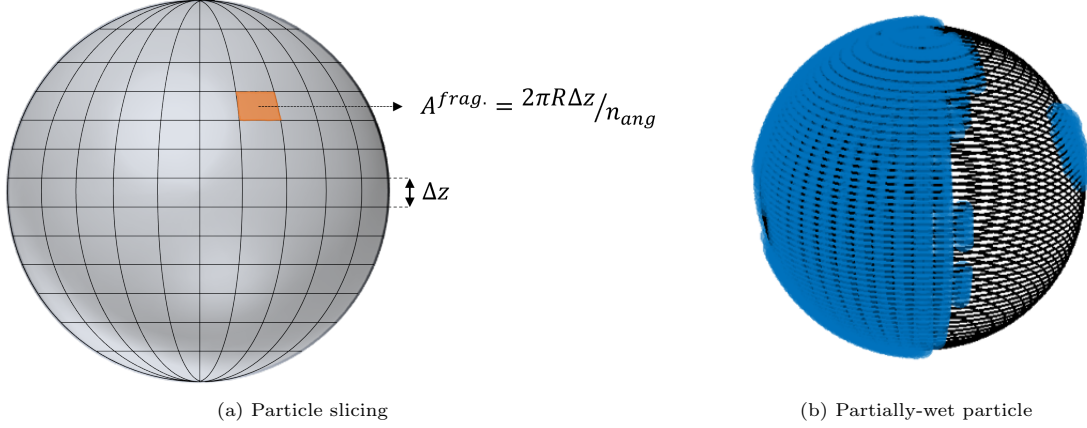(a) Particle slicing   (b) Partially-wet particle

Figure 8: A schematic representation of particle surface fragments (a), and an example of the liquid distribution on this surface (b).

is flooded with liquid to completely fill all void spaces. Subsequently, the column is inserted into the MRI scanner, and MRI flow imaging is performed on the single-phase flow. Following that, gas flow is introduced into the column, and after a waiting period of a few minutes to allow the flow to stabilize, MRI flow imaging is conducted on the two-phase flow. Based on the obtained local liquid velocity field, it becomes feasible to examine the variations in liquid velocity distribution between single-phase liquid and two-phase trickling flow.

From a PCGRE scan, two types of images are extracted: signal intensity and phase images. In this sequence, the velocity value of each voxel is calculated by measuring the signal phase shift in that voxel. This is done by applying a bipolar gradient in the direction of the flow. By applying this gradient, stationary liquid will have a zero signal phase change, but moving liquid will experience a signal phase change that is linearly related to its velocity. The method used in this research to implement the PCGRE sequence is the so-called flow compensation technique [51]. In this technique, two scans are acquired from the flow. The first scan is performed without applying the bipolar gradients, and it is called the reference scan. No velocity encoding is applied in this scan, and it only includes the background signal phase image. The second scan that is performed with the bipolar gradients includes both the background signal phase image and the signal phase changes because of the velocity. By subtracting the first scan from the second scan, the background signal phases are removed, and a map of signal phase changes due to the velocity is obtained.

Finally, the obtained signal phase map is converted into a velocity map by defining a proper velocity encoding (*venc*) factor value. The *venc* is defined in a way that it represents the highest velocity value inside the flow imaging domain to avoid phase-wrapping artifacts [52, 53]. Here, a *venc* of 20 cm/s is used as an assumption for the order of the maximum velocity. A signal phase-unwrapping function is also applied for the possibility of signal phase aliasing

11

(phase wrapping) because of too high velocities. [54, 55]

The intensity images are binarized, and a mask is created from them. The binarization is done by defining a threshold value at each cross-sectional slice. This mask is later used to eliminate the noise from the phase image by multiplying the signal phase image with the mask. Finally, the 3D velocity map is extracted from the 3D masked signal phase image. The obtained 3D velocity map is corrected to account for conservation of mass in a way that the sum of the voxel flow rates at each cross-sectional slice should correspond to the inlet liquid flow rate. The correction is done by a uniform correction of all voxel values based on the difference between the average superficial velocity at that slice and the superficial inlet velocity.

3. Results and Discussion

3.1. Saturation field

Figure 9 provides a qualitative overview of the 3D liquid distribution imaged under three different flow conditions. Figures 9(a) and (b) show the liquid distribution in the case of single-phase liquid flow and two-phase gas-liquid flow, respectively. These images are later used for the calculation of the saturation field. The static liquid hold-up in a trickle bed is assessed by stopping the liquid flow and only allowing the gas flow inside the column. After waiting a few minutes to remove all the non-static liquid, the MRI imaging is performed. Figure 9(c) represents the 3D visualization of the static liquid hold-up.

To evaluate the quality and reliability of obtained MRI structural images, the Signal-to-Noise Ratio (SNR) is calculated. SNR represents the ratio of signal strength to the noise level present in the image. Noise encompasses unwanted random variations and interference originating from various sources such as thermal noise, electronic noise, motion, susceptibility variations, and radio-frequency (RF) interference. SNR is computed by dividing the signal magnitude by the standard deviation of the noise within the image. A higher SNR value indicates a more pronounced and distinguishable signal in relation to the noise, thereby indicating a higher-quality MRI image.

To calculate the SNR, the following steps are taken. First, four ROIs (region of interest) are identified within the image, where a uniform liquid phase is present and from which the signal is obtained. The mean signal intensity within these regions is then calculated. Second, another four regions are defined within the image where there is minimal or no signal (referred to as the noise region). The noise regions are selected to be outside the column, containing only background noise. The standard deviation of the voxel intensities within the noise regions is computed and averaged over the four regions. Finally, the SNR is obtained by dividing the mean signal intensity in the ROIs by the average standard deviation in the noise regions. The SNR value in the acquired structural images is determined to be approximately 29 for a cross-sectional slice in the single-phase image and 26 for the same cross-sectional slice in the two-phase image. These SNR values suggest that the signal in the image is more

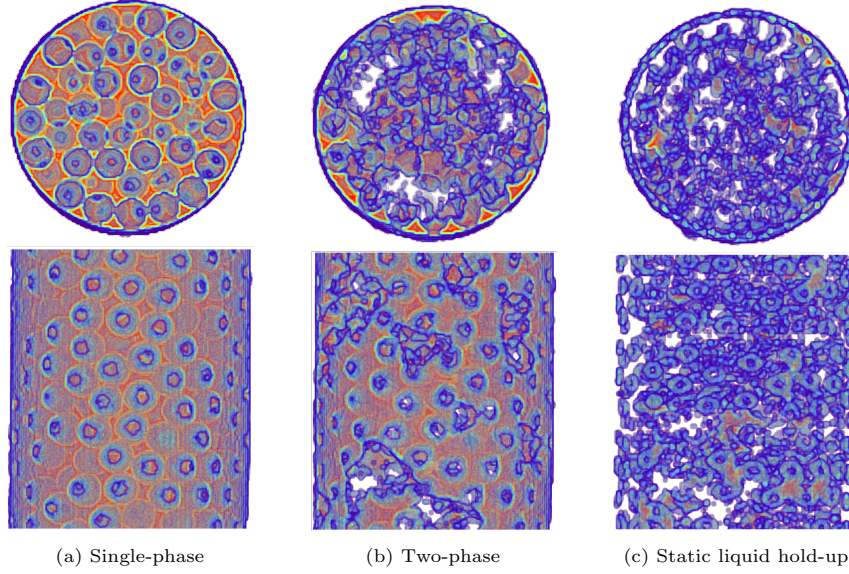(a) Single-phase   (b) Two-phase   (c) Static liquid hold-up

Figure 9: 3D structure images of the liquid distribution in a single-phase liquid flow (a), two-phase gas-liquid flow (b) and the static hold up (c).

than 25 times stronger than the noise. This observation suggests a high level of signal quality, wherein the image exhibits a distinct and well-defined signal that is readily discernible from the accompanying noise.

3.1.1. Axial saturation field for varying liquid flow rates

Figure 10 shows the changes in the axial liquid saturation field by increasing the liquid superficial velocity. The liquid flow rate is increased while halting the gas flow until the liquid flow rate reaches the specified value, and subsequently reintroducing the gas flow. After a brief waiting period of a couple of minutes to allow for flow stabilization, the imaging procedure is performed. It can be seen that by increasing the liquid flow rate, the saturation value increases.

In the undeveloped region, indicated by S_1 in Figure 10, the average saturation values are higher at higher liquid velocities. By moving along the column and entering S_2, the developing region, the saturation decreases along the axial direction. This decrease is steeper for the higher liquid flow rates. This decrease in the axial saturation values continues up to the start of the region S_3, the developed region, after which the saturation values remain approximately constant along the axial direction. In this figure, the saturation profile at the liquid superficial velocity of zero (static) indicates the static saturation in the column. For the 3 mm polypropylene spheres, a value of 7.0% is measured for the average static liquid saturation.
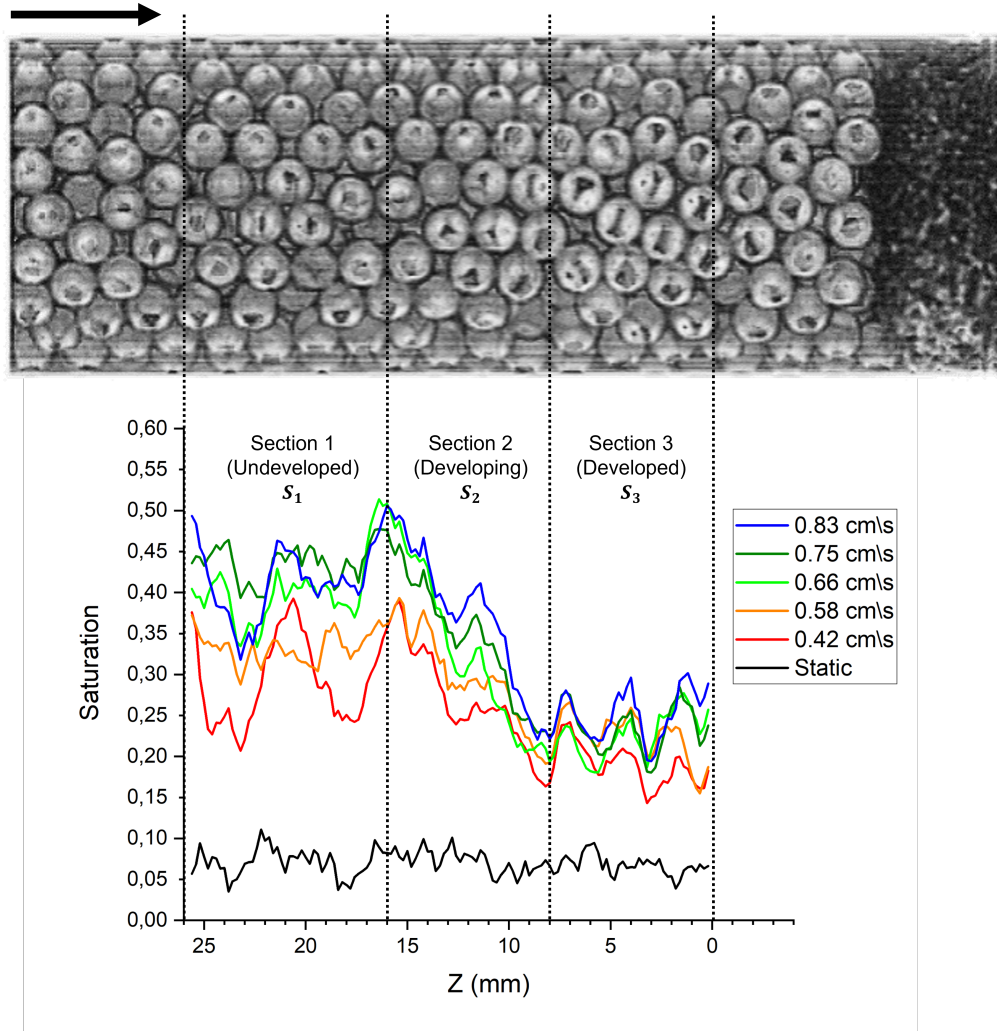
13

Figure 10: A reconstructed MRI image of the bed structure and axial liquid saturation profiles at varying liquid superficial velocities and a constant gas superficial velocity of 1 cm/s.
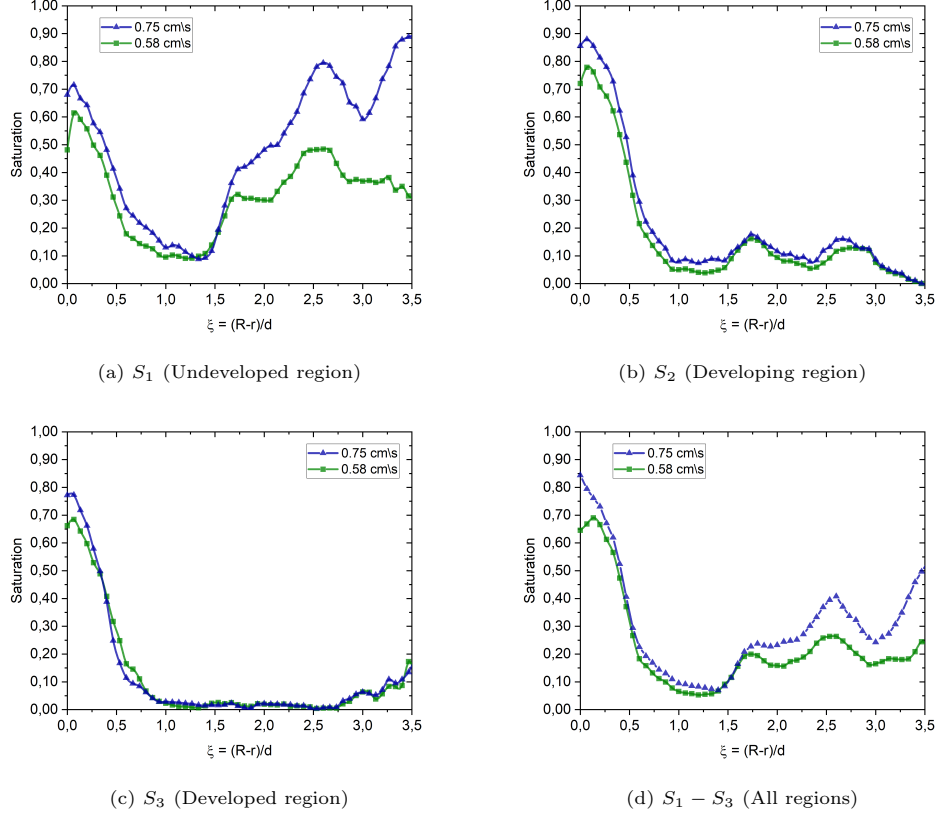
(a) S_1 (Undeveloped region)

(b) S_2 (Developing region)

(c) S_3 (Developed region)

(d) $S_1 - S_3$ (All regions)

Figure 11: Average radial profiles of liquid saturation in different axial sections.

3.1.2. Radial average saturation profile

To further investigate the local saturation field and liquid spread in a trickle bed, the radial average saturation profiles, averaged over the S_1, S_2 and S_3 sections, are calculated for two different liquid superficial velocities. Figure 11(a) shows these radial saturation profiles averaged over the S_1 section plotted against the dimensionless distance from the column wall (ξ), for liquid superficial velocities of 0.58 cm/s and 0.75 cm/s. Similarly, Figure 11(b) and Figure 11(c) show the radial saturation profiles averaged over the S_2 and S_3 sections, respectively.

It is evident from Figure 11 that the saturation value near the column wall (($\xi < 0.5$)) is high in all the three sections, and it becomes even higher at higher liquid flow rates. This phenomenon can be attributed to two factors. First, in slender tubes, the porosity near the column wall is higher, resulting in lower hydraulic resistance for the pores near the column compared to those in the inner region of the column. As a result, the liquid flow tends to preferentially move from these regions towards the wall. This preferential distribution of the liquid causes the maldistribution of the phases. The preferential flow of liquid in

15

slender packed bed columns has been readily discussed in the literature [56, 57].

The second reason for the high saturation close to the column could be related to the materials used and their contact angle. The spreading behavior of the liquid is influenced by the wetting properties of the solid surface. If the liquid wets the solid surface well, it tends to spread more easily. The particles used here are polypropylene spheres with a contact angle of approximately 105 degrees [58], while the column material is polycarbonate with a contact angle of approximately 88 degrees [59]. The relatively lower contact angle of the column wall makes it more hydrophilic than the particles, resulting in an uneven distribution of flow.

In the S_1 region (Figure 11(a)), the saturation values in the center of the column ($1.5 < \xi < 3.5$) are observed to be high. These values are even higher for higher liquid superficial velocities. The reason for this is that the liquid flow is introduced at the center of the column. Moving to the S_2 region (Figure 11(a)), the saturation value in the center of the column decreases. This is due to the fact that the liquid flow, introduced at the center of the column, needs some distance to move towards the wall region where it prefers to be. Figure 11(c) displays the radial saturation profile in the S_3 region. Here, the liquid is mostly directed towards the wall region, where the low hydraulic resistance makes it a preferable path for the liquid flow to pass through. Lastly, Figure 11(d) presents the radial liquid saturation profile averaged over all the sections.

3.1.3. Axial particle wet-perimeter profile

Figure 12 shows the axial particle wet-perimeter profile along the column for seven different liquid superficial velocities. This figure shows how the particle wet-perimeter at each cross-sectional slice changes along the column length. It is noticeable that the variation of the particle wet-perimeter field along the column follows more or less the same trend as the variation of the liquid saturation field along the column length (shown in Figure 10). By increasing the liquid superficial velocity, the wetting perimeter starts to increase. This increase is more significant in S_1 due to the effect of the inertia forces. Moreover, beyond a certain liquid superficial velocity, changes in the wet-perimeter become less pronounced. For example, in Figure 12, the particle wet-perimeter profiles at liquid superficial velocities of 0.66, 0.75, and 0.83 cm/s are close to each other.

3.2. Particle wet area

As discussed in the previous sections of this paper, a novel methodology has been developed to determine the wet-area fraction of particles and its 3D distribution throughout the column using the MRI structure images of both single-phase and two-phase flows.

3.2.1. Validation of wetting profiles

In order to test the validity of the particle wetting area profiles, the particle wet-area calculation is performed on the single-phase image. From the single-phase image, it is expected to have full particle wetting. The analysis, however,
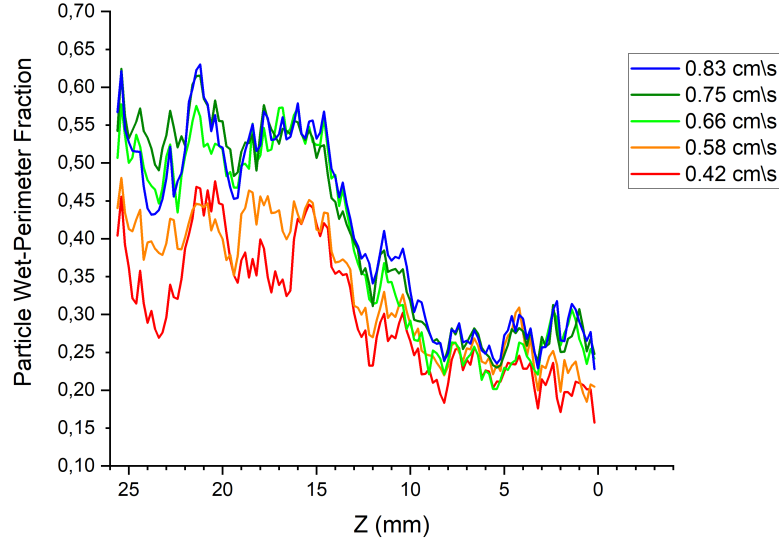
Figure 12: Axial particle wet-perimeter profiles at varying liquid superficial velocities and a constant gas superficial velocity of 1 cm/s.
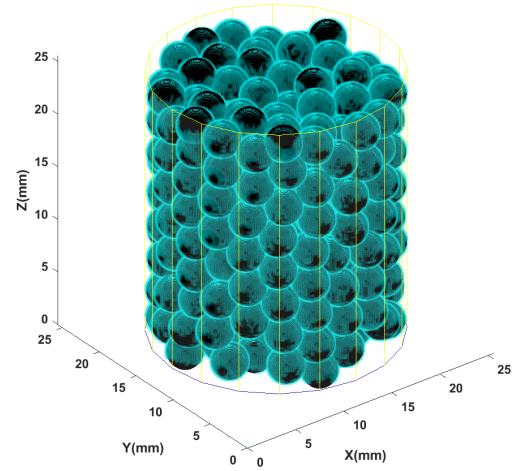
shows an average 92% particle wet-area fraction for the single-phase flow. This is because of the limitations of MRI to represent the liquid voxels in the regions where there is contact between a particle with another particle or with the column wall. This can be seen clearly in Figure 13. Figure 13 provides a 3D representation of the particle wetting and the average radial particle wet-area fraction profile for a single-phase liquid flow and a two-phase flow of 0.75 cm/s liquid and 1 cm/s gas superficial velocities. Observations from the single-phase case reveal that particle surface fragments touching to the column wall are designated as dry regions due to a lack of sufficient signal intensity in these voxels to be classified by the binarization method as liquid using MRI. To quantify this effect, the radial profile of the average particle wet-area fraction is plotted in Figure 13(c).
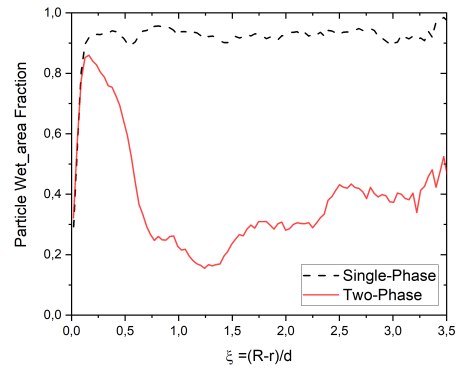
3.2.2. Particle wet area fraction distribution

By calculating the wet-area fraction of each particle, it is possible to investigate how the average particle wet-area fraction varies at different radial and axial locations inside the trickle column. In order to investigate this position dependence, the column is divided into nine sections, i.e. three sections in the radial direction and three in the axial direction. Figure 14 shows how the column is divided. The axial sections are S_1, S_2, and S_3, similar to the sections used in Figure 10. The radial sections are R_1, R_2, and R_3, and are defined based on the particle's center distribution; the R_1 section includes the particles adjacent to

17
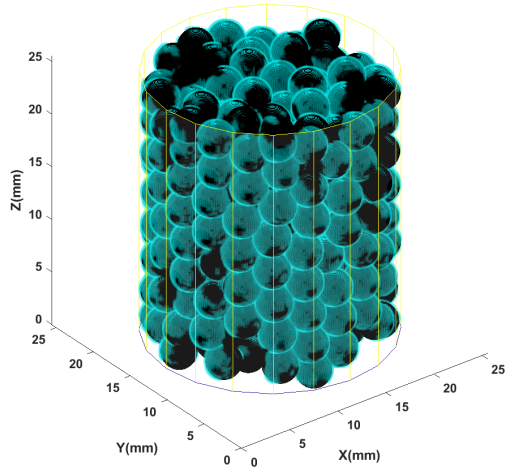
(a) Two-phase flow.

(b) Single-phase flow.

(c) Radial particle wet-area profile.

Figure 13: A 3D schematic of the particle wetting area, colored in blue, inside the trickle bed (a,b) and the radial averaged particle wet-area fraction profiles (c) in the case of the single-phase and the two-phase flow.

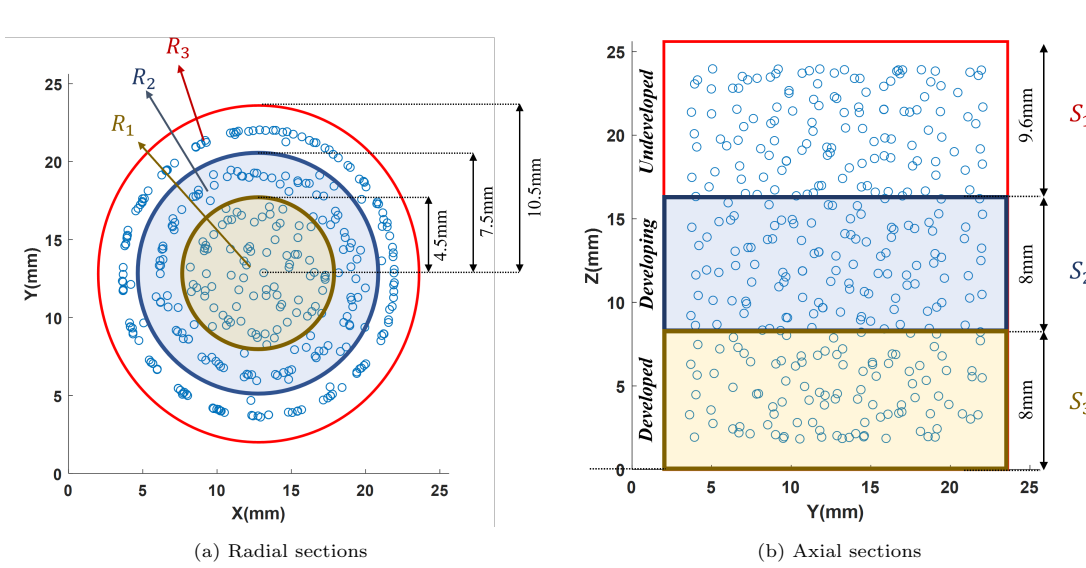(a) Radial sections   (b) Axial sections

Figure 14: The division of the trickle column in the radial (a) and axial (b) direction. The blue empty circles show the particle centers.

the column wall; the R_2 section contains the second radial layer of the particles close to the column wall; and the R_3 section consists of the particles located in the radial center of the column.

Figure 15 shows the relative frequency of the particle wet-area fraction distribution at different axial and radial sections for a two-phase flow of 0.75 cm/s liquid and 1 cm/s gas superficial velocities. It can be seen that along the axial direction (flow direction), the particle wet-area fraction decreases, which is in line with the axial saturation profile of Figure 10. In the radial direction, R_2 has the lowest particle wetting, and the particles close to the column wall (R_3) have the highest fraction of wetting. The average particle wet-area fractions at the nine sections of the column are calculated and tabulated in Table 1. The results shown in this table reveal that the intersection of the R_2 and the S_3 regions has the lowest particle wet-area fraction with an average value of 7%, and the intersection of R_1 and S_1 (center of the column at the inlet) has the highest particle wet-area fraction with an average value of 76%, complying with the radial saturation profiles in Figure 11.

3.2.3. Radial particle wet-area fraction profiles

From the radial liquid saturation profiles, it can be seen that most of the liquid flows through the void regions between the column wall and the adjacent particles, and there is a preferential distribution of the liquid. In order to investigate the effect of preferential distribution on the particle wetting, the

19

(a) S_1 (b) S_2 (c) S_3

(d) R_1 (e) R_2 (f) R_3
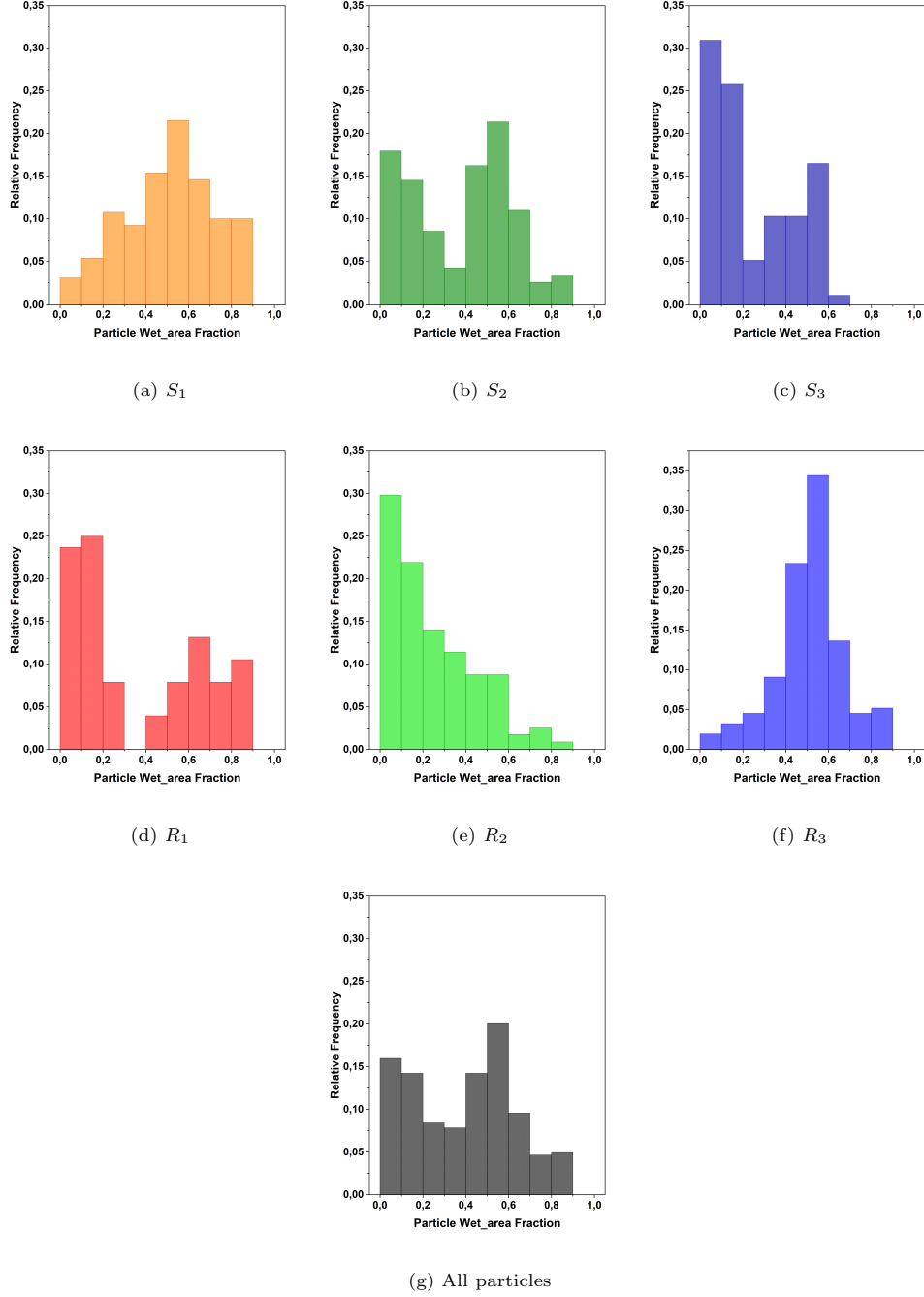
(g) All particles

Figure 15: The relative frequency of particle wet-area fraction distribution at the three axial and the three radial sections.

Table 1: Average particle wet area percentage at each section of the column.

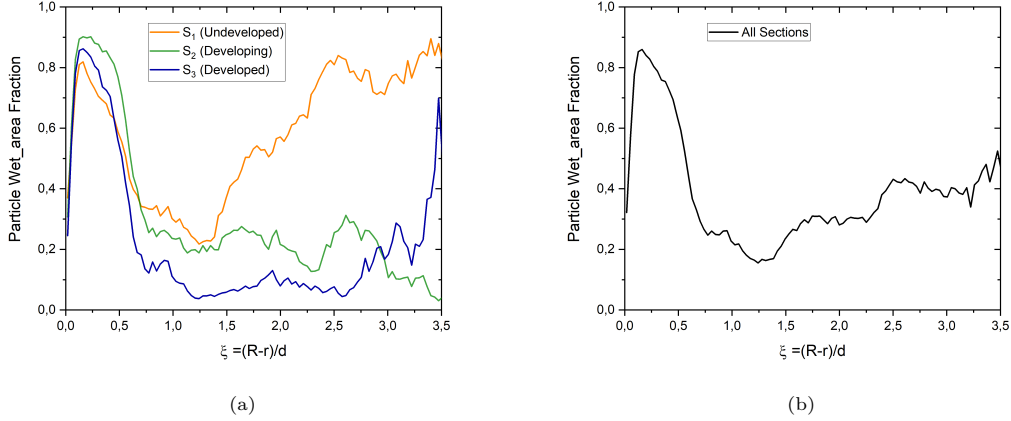| Axial/Radial	R_1	R_2	R_3	Total
S_1	76%	40%	50%	52%
S_2	19%	23%	55%	38%
S_3	12%	7%	42%	24%
Total	38%	24%	49%	39%

(a)

(b)

Figure 16: Radial particle wet area profile at the three different axial sections: S_1, S_2, and S_3 (a) and averaged over all the sections (b).

column cross-section is divided into 100 radial bins, and the radial particle wet-area fraction profile is calculated. Figure 16 shows the radial dependency of the particle wet-area fraction at the different axial sections. Comparing this figure with Figure 11 shows that the radial wetting profile follows the trend of the radial liquid saturation profile, where the particles close to the column wall are more wetted.

3.2.4. Average local wetting of the particle surface

It is noticeable from the radial wet-area fraction profiles in Figure 16 that at ξ values slightly higher than 0.5 (half particle distance from the wall), there is a sharp decrease in the particle wetting. This implies that there is a directionality of the particle wetting. In other words, a certain direction of the particle surface is more prone to be wet, and there is a sort of preferential surface wetting direction resulting from the preferential liquid phase distribution. In order to investigate this in more detail, the average surface wetting distribution of the particles is calculated. The average surface wetting distribution is the probability of each surface fragment being wet in different particles.

For points on the particle surface, an azimuthal angle θ is used that is defined such that $\theta = 0$ corresponds to the points closest to the column wall and $\theta = \pi$ to

(a) Two-phase (3D view)   (b) Two-phase (top view)

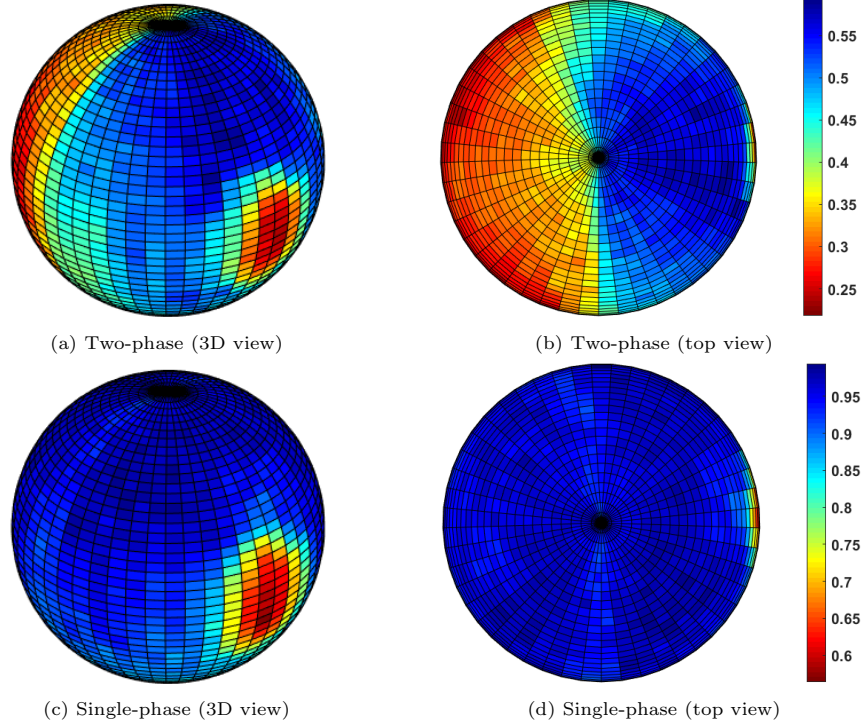(c) Single-phase (3D view)   (d) Single-phase (top view)

Figure 17: 3D and top view of the average surface wetting distribution of the particles surface fragments in a two-phase (a,b) and a single-phase (c,d) flow.

the points closest to the column center. This allows us to average over the surface wetting distributions of all particles at different positions with corresponding azimuthal angles θ to the column wall. This means that, if we define points in spherical coordinates with respect to fixed x, y, z directions, the spheres are rotated around the z axis before averaging. If we consider reference frames with fixed x, y, z directions, with θ_c the azimuthal angle of a particle's center with respect to a reference frame with its origin on the column center line, and θ_s the azimuthal angle of a point on the particle surface with respect to a reference frame with its origin at the particle center, then $\theta = \theta_s - \theta_c$. Figure 17 shows the average surface wetting distribution of the particle surface fragments in the case of a two-phase and single-phase flow. In both the single and the two phase flow a higher probability of non-wetting is found at the column wall, which was previously discussed in Figure 13.

It can be seen from Figure 17 that in a two-phase flow, some parts of the particles surface have a higher chance of wetting. To further investigate the dependence of the directionality of the particle wetting to the location of the particle inside the column, the wetting probability profiles are calculated for the particles at the three different radial sections (R_1, R_2, and R_3). Figure 18 shows the azimuthal wetting probability profile, averaged over the particle height,
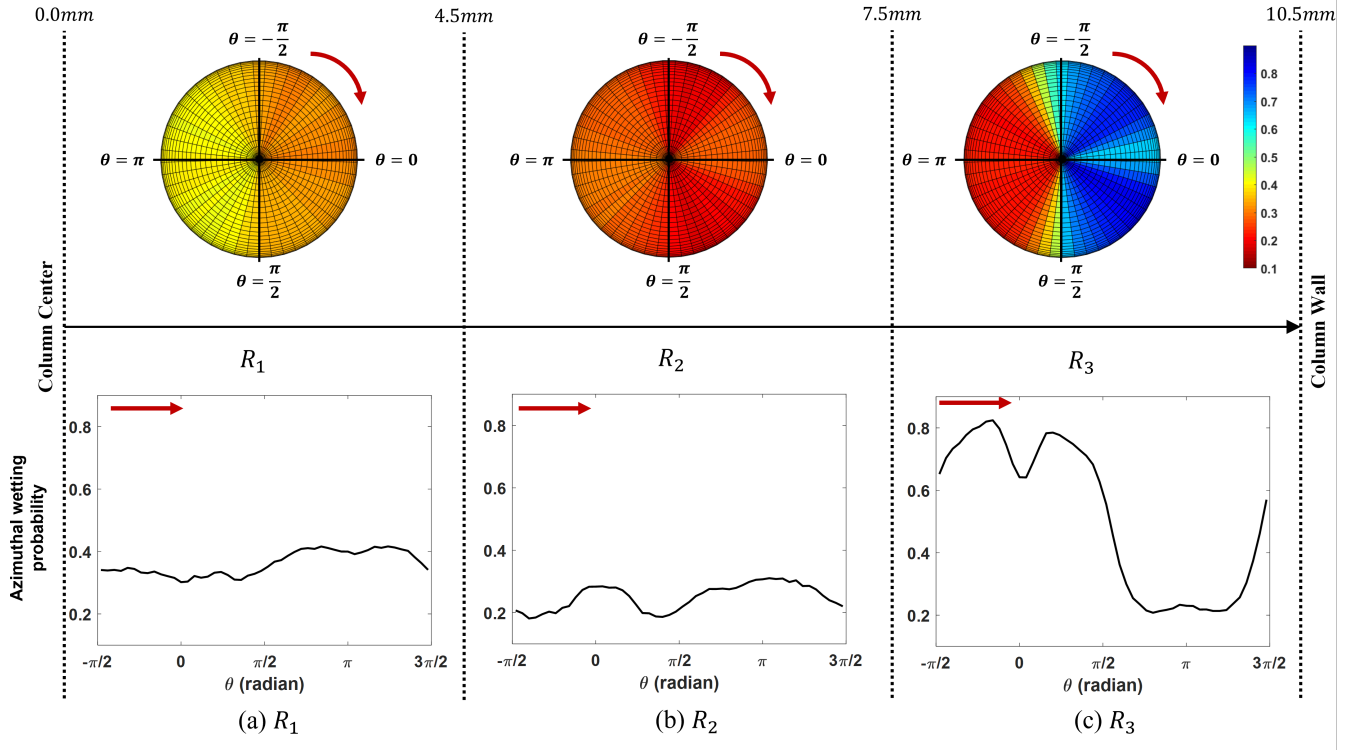
22

Figure 18: Azimuthal wetting probability profile of the particles at the three radial sections: R_1 (a), R_2 (b), and R_3(c).

and Figure 19 shows the zenithal wetting probability profile, averaged over the azimuthal angle θ, at the three radial sections.

It can be seen from Figure 18 that for the particles in R_3, the surface fragments facing the wall are more prone to be wet compared to the ones facing the center of the column, and the difference in azimuthal wetting probability distance between these two face is substantial ($\approx$60%). The surface fragments touching the column wall (the red circular region in Figure 17) have a lower wetting probability. This is also true in the case of single-phase flow, because of the experimental limitations discussed in the method validation section. For the particles in the inner radial regions of R_1 and R_2, the surface of the particle facing radially inward, i.e., the column center, is wetter, but the difference is comparatively negligible ($\approx$10%).

The zenithal wetting probability profiles at the three radial sections are shown in Figure 19. The zenithal wetting probability in the three radial sections follows a similar trend. The variation in the zenithal wetting probability is not significant along the particle height. The top part of the particle is $\approx$10% more prone to be wet than the bottom of the particle. Figure 20 shows the azimuthal
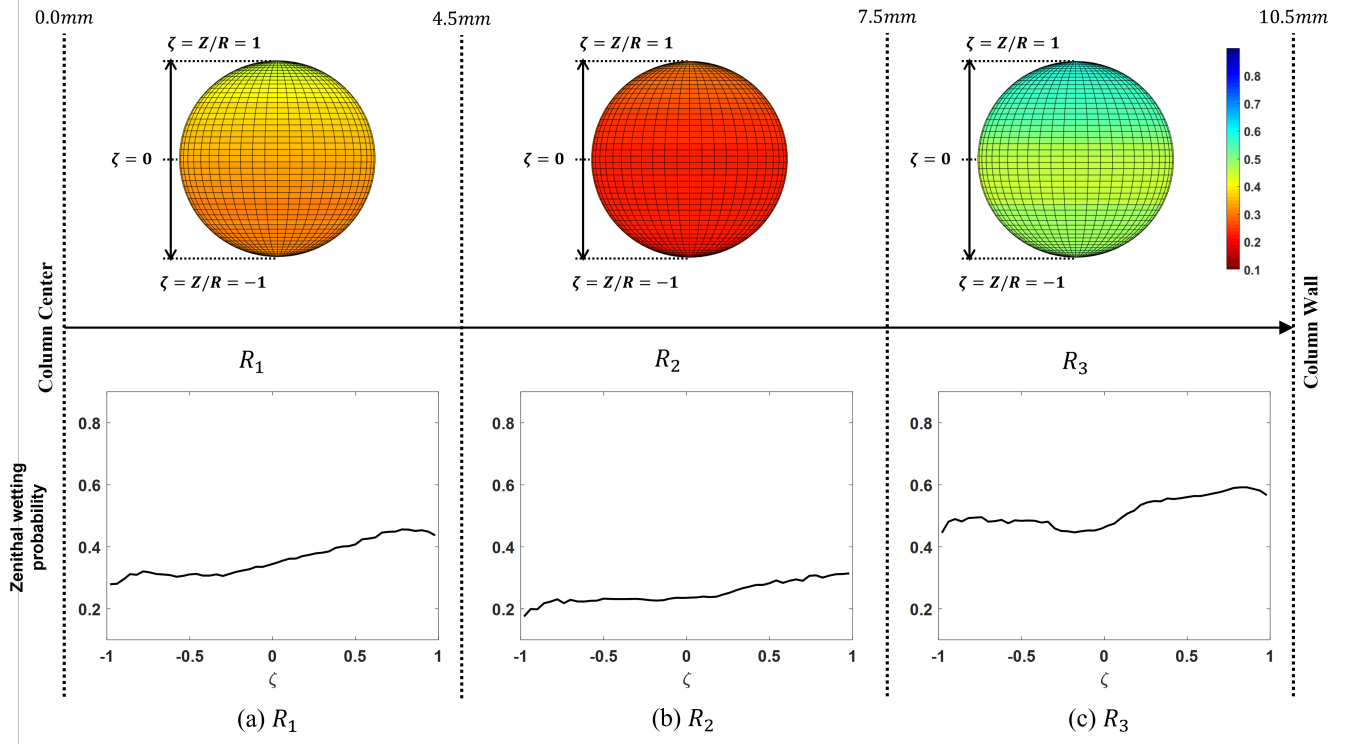
23

Figure 19: Zenithal wetting probability profile of the particles at the three radial sections: R_1 (a), R_2 (b), and R_3(c).
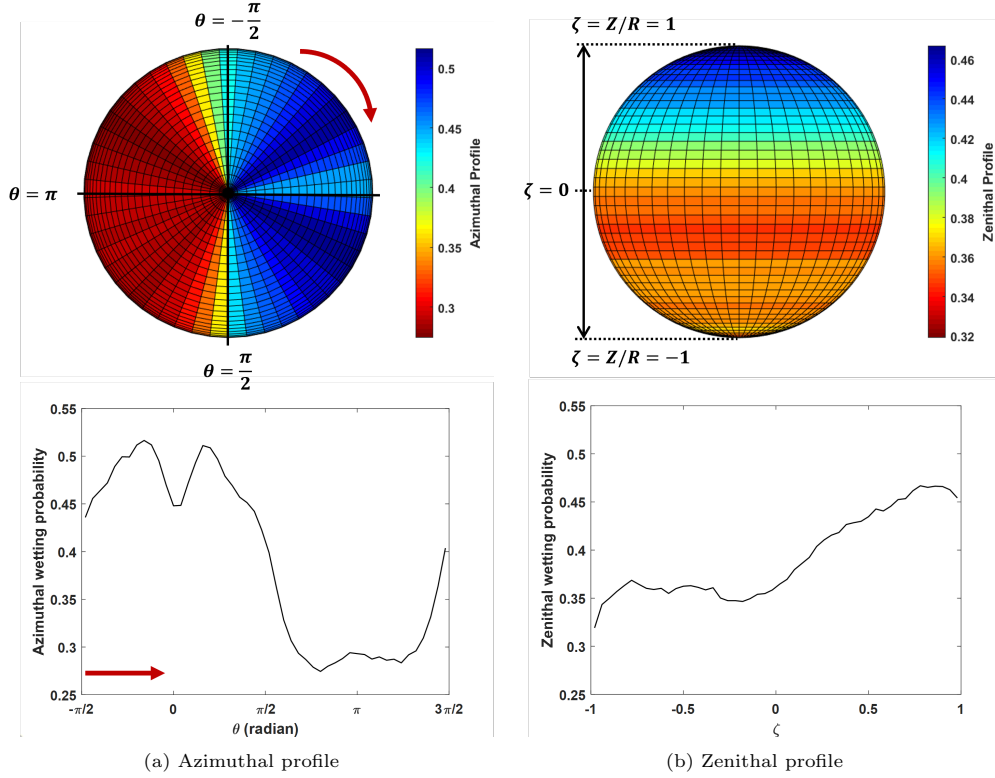
Figure 20: Azimuthal (a) and zenithal (b) wetting probability profiles averaged over all the particles inside the trickle bed.

and zenithal wetting probability profiles averaged over all the particles inside the trickle bed. From these profiles, a preferential wetting direction of the particles' surface is observable. The surface fragments facing the column wall are ≈25% wetter than the ones facing the center of the column. This is because, in slender trickle columns, there are much more particles near the wall, than near the center. Also, the surface fragments at the top of the particles have ≈10% higher probability of wetting compared to ones at the bottom of the particles.

3.3. Flow field

Another characteristic for the liquid distribution inside a trickle bed is the liquid flow field, described by the parameters; liquid velocity and flow rate distribution inside the column. Figure 21 shows the velocity distribution of the liquid flow in a cross-sectional slice in a single-phase and in a two-phase flow obtained from the MRI flow images. MRI enables the voxel-to-voxel comparison of the liquid velocity field. The comparison of Figures 21(a) and (b) illustrates how the local liquid velocities change by introducing the gas flow. It is evident that there is a sharp increase in the local liquid velocities at some locations. This

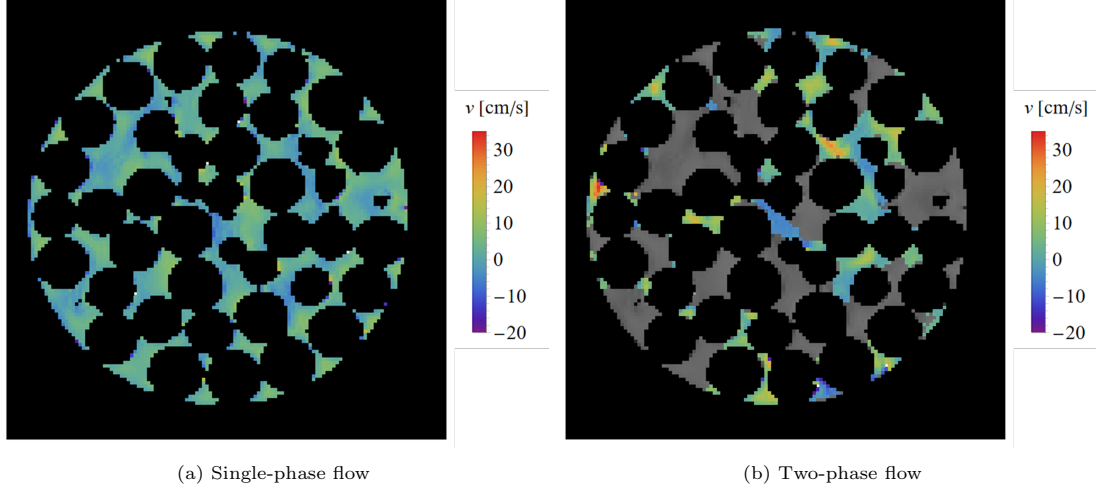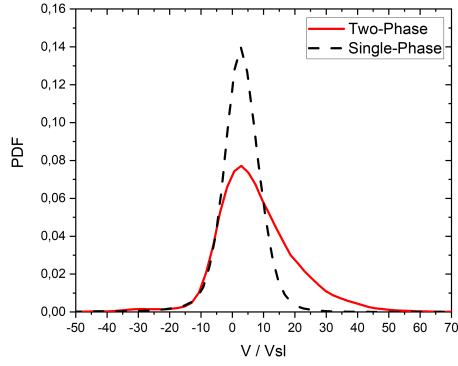(a) Single-phase flow   (b) Two-phase flow

Figure 21: Liquid velocity distribution in a cross-section of the column: (a) single-phase flow with a liquid superficial velocity of 0.52 cm/s and (b) two-phase flow with a liquid superficial velocity of 0.52 cm/s and a gas superficial velocity of 1 cm/s. The gray voxels are showing the gas phase.

makes sense as by introducing the gas flow, a major fraction of the column's void volume is being occupied by the gas phase, decreasing the cross-sectional area for the liquid to pass through. In order to quantify the uniformity of the velocity field, the probability density functions (PDF) of the liquid voxel velocities for both single-phase and two-phase flow are plotted in Figure 22(a). It is noticeable that the velocity distribution is broader in the two-phase flow, meaning that a more significant number of high velocities is present in the two-phase flow compared to the single-phase flow, complying with the findings in Figure 21. Both the two-phase and single-phase flows have a peak near zero velocity, and the peak is higher and steeper in the single-phase flow.

To characterize the distribution of the liquid flow, the radial dimensionless superficial velocity profile (Figure 22(b)) is plotted. This is done by binning the column cross-section into 54 radial bins. Figure 22(b) shows the average velocity values of liquid flow at each bin averaged over the column length and divided by the inlet superficial liquid velocity plotted versus the dimensionless distance from the column wall (ξ). At lower ξ values, there is a sharp increase in the average velocity, resulting in the channelling of the liquid flow close to the column wall. To further investigate the flow distribution, the radial cumulative dimensionless flow rate profile (Figure 22(c)) with respect to the dimensionless distance from the wall is plotted. In this figure, at lower ξ values, there is a large jump in the cumulative flow rate, meaning that approximately 50% and 35% of the liquid flow is passing through the void area close to the column wall in the two-phase and single-phase flows, respectively. The second jump occurs at the second radial layer of the particles ($0.5 < \xi < 1.5$), and approximately 25% and
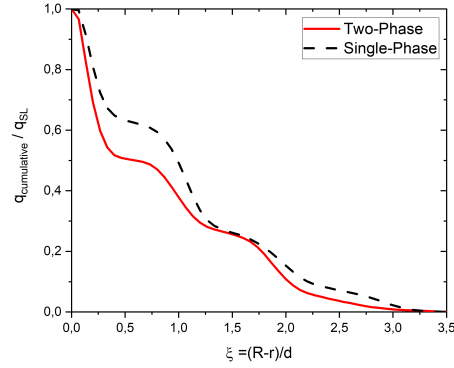
(a) PDF of velocity distribution.
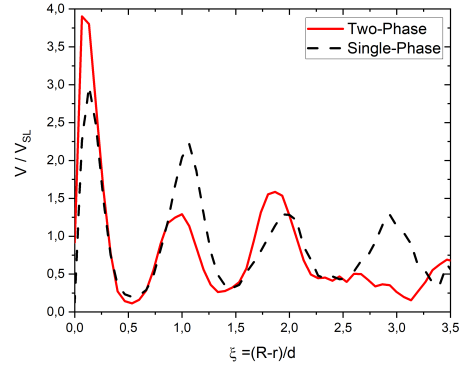
(b) Radial velocity profile.

(c) Cumulative flow rate profile.

Figure 22: PDF of the velocities of liquid voxels in the column (a), radial dimensionless velocity profile (b) and radial cumulative flow rate profile (c) for a single-phase flow with a liquid superficial velocity of 0.52 cm/s and a two-phase flow with a liquid superficial velocity of 0.52 cm/s and a gas superficial velocity of 1 cm/s.

40% of the liquid flow moves through this region in the two-phase and single-phase flows, respectively. This means that there is a shift towards more liquid passing near the column wall and more intense preferential flow distribution for two-phase flow.

4. Data Availability and Reproducibility Statement

A complete data package, containing results in both Matlab .fig and .csv formats, is openly accessible through the 4TU data repository at the DOI link: doi:10.4121/ee89efa0-edd0-4a9e-8982-cdd38a15bae8. For MRI scans, the data is provided in the .raw format and can be viewed using the 3D Volume Viewer plugin (Version 2.0) of the ImageJ software (Version 1.54c). Additionally, detailed readme.txt files accompany each figure in the paper, offering comprehensive instructions for accurate figure reproduction.

Throughout the experimentation process, we ensured pre-wetting of the column with pure liquid flow before each two-phase experiment, while meticulously removing any bubbles. The data sets were measured twice, and although minor variations resulted from the MRI scanner's column positioning, qualitatively consistent findings revealed the same preferential flow near the column walls in both cases. Our averaging procedures effectively accounted for individual experiment variations, providing a reliable representation of liquid distributions in our research.

5. Conclusion and outlook

In this research, MRI is used to investigate the two-phase gas-liquid flow behavior in a slender trickle column. The 3D liquid distribution is characterized using three parameters: saturation, particle wetting, and flow fields. The results showed that there is a preferential distribution of liquid in the column, with most of it present close to the wall. One of the ways for preventing such a maldistribution is to use flow re-distributors at certain axial positions along the slender trickle bed column. Furthermore, a novel method has been developed in this research to calculate the wetted area of individual particles in a trickle bed. The preferential distribution of liquid in the column gives rise to the preferential surface wetting of the particles, with the part of the surface that faces the column wall being more prone to be wet than the surface facing column center. Finally, the MRI flow images show higher velocities, close to the wall, resulting in a stronger wall channeling of liquid compared to the single-phase flow.

Validation of the particle wetted area calculation method showed a 92% wetting fraction for the single-phase flow. This is because of the limitation of MRI in capturing the liquid voxels in the areas where there is contact between the particles and the column wall. One method for correcting this error can be treating the non-wet areas in the single-phase case as wet areas due to the presence of high capillary effects in those regions and considering the fact that the

column was initially in pre-wet condition. To gain a more comprehensive understanding of these regions, obtaining higher resolution images in the relevant areas is required.

This study offers valuable insights into the two-phase gas-liquid flow behavior in a slender trickle column. MRI, as a non-invasive tool, helps detailed understanding, visualizing, and characterizing of two-phase flow behavior in trickle bed reactors, which can contribute to more efficient and optimized design of such reactors. The resulting detailed experimental data sets can also contribute to the validation of detailed hydrodynamic models that are used for simulating the two-phase flow in trickle columns. The developed method for calculating the wetted area of spherical particles can be extended to encompass non-spherical particles, which have extensive applications in various industrial trickle beds.

6. Acknowledgement

References

[1] A. J. van Houwelingen, C. Sandrock, W. Nicol, Particle wetting distribution in trickle-bed reactors, AIChE journal 52 (10) (2006) 3532–3542.

[2] V. V. Ranade, R. Chaudhari, P. R. Gunjal, Trickle bed reactors: Reactor Engineering and Applications, Elsevier, 2011.

[3] D. Nguyen, V. Balakotaiah, Flow maldistributions and hot spots in down-flow packed bed reactors, Chemical Engineering Science 49 (24) (1994) 5489–5505.

[4] S. Zimmerman, K. Ng, Liquid distribution in trickling flow trickle-bed reactors, Chemical Engineering Science 41 (4) (1986) 861–866.

[5] B. Qi, S. Uribe, O. Farid, M. Al-Dahhan, Random trilobe packing using rigid body approach and local Gas-Liquid hydrodynamics simulation through CFD with experimental validation, Chemical Engineering Journal 435 (2022) 134481.

[6] H. Bouras, Y. Haroun, F. F. Bodziony, R. Philippe, P. Fongarland, F. Augier, Use of CFD for pressure drop, liquid saturation and wetting predictions in trickle bed reactors for different catalyst particle shapes, Chemical Engineering Science 249 (2022) 117315.

[7] H. Deng, B. Guo, H. Dong, C. Liu, Z. Geng, Computational investigation of liquid holdup and wetting efficiency inside trickle bed reactors with different catalyst particle shapes, Applied Sciences 10 (4) (2020) 1436.

[8] A. S. Ambekar, U. Rüde, V. V. Buwa, Forces governing the dynamics of liquid spreading in packed beds, Journal of Fluid Mechanics 948 (2022) A13.

[9] A. S. Ambekar, U. Rüde, V. V. Buwa, Particle-resolved simulations of local liquid spreading in packed beds: Effect of wettability at varying particle size, Physics of Fluids (2022).

[10] F. Augier, A. Koudil, A. Royon-Lebeaud, L. Muszynski, Q. Yanouri, Numerical approach to predict wetting and catalyst efficiencies inside trickle bed reactors, Chemical Engineering Science 65 (1) (2010) 255–260.

[11] R. J. Lopes, R. M. Quinta-Ferreira, Three-dimensional numerical simulation of pressure drop and liquid holdup for high-pressure trickle-bed reactor, Chemical Engineering Journal 145 (1) (2008) 112–120.

[12] R. J. Lopes, R. M. Quinta-Ferreira, Assessment of CFD Euler–Euler method for trickle-bed reactor modelling in the catalytic wet oxidation of phenolic wastewaters, Chemical Engineering Journal 160 (1) (2010) 293–301.

[13] Z. Solomenko, Y. Haroun, M. Fourati, F. Larachi, C. Boyer, F. Augier, Liquid spreading in trickle-bed reactors: Experiments and numerical simulations using Eulerian–Eulerian two-fluid approach, Chemical Engineering Science 126 (2015) 698–710.

[14] Y. Wang, J. Chen, F. Larachi, Modelling and simulation of trickle-bed reactors using computational fluid dynamics: A state-of-the-art review, The Canadian Journal of Chemical Engineering 91 (1) (2013) 136–180.

[15] A. Gianetto, V. Specchia, Trickle-bed reactors: state of art and perspectives, Chemical Engineering Science 47 (13-14) (1992) 3197–3213.

[16] P. R. Gunjal, M. N. Kashid, V. V. Ranade, R. V. Chaudhari, Hydrodynamics of trickle-bed reactors: experiments and CFD modeling, Industrial & Engineering Chemistry Research 44 (16) (2005) 6278–6294.

[17] P. L. Mills, M. P. Dudukovic, Evaluation of liquid-solid contacting in trickle-bed reactors by tracer methods, AIChE Journal 27 (6) (1981) 893–904.

[18] Z. Cihla, O. Schmidt, A study of the flow of liquid when freely trickling over the packing in a cylindrical tower, Collection of Czechoslovak Chemical Communications 22 (3) (1957) 896–907.

[19] A. K. Saroha, K. D. P. Nigam, A. K. Saxena, V. K. Kapoor, Liquid distribution in trickle-bed reactors, AIChE journal 44 (9) (1998) 2044–2052.

[20] M. Li, Y. Bando, K. Suzuki, K. Yasuda, M. Nakamura, Liquid flow rate distribution in trickle bed with non-uniformly packed structure, Journal of Chemical Engineering of Japan 33 (2) (2000) 211–216.

[21] C. Marcandelli, A. Lamine, J. Bernard, G. Wild, Liquid distribution in trickle-bed reactor, Oil & Gas Science and Technology 55 (4) (2000) 407–415.

[22] A. Kundu, A. K. Saroha, K. D. P. Nigam, Liquid distribution studies in trickle-bed reactors, Chemical Engineering Science 56 (21-22) (2001) 5963–5967.

[23] A. Atta, S. Roy, K. D. P. Nigam, Investigation of liquid maldistribution in trickle-bed reactors using porous media concept in CFD, Chemical Engineering Science 62 (24) (2007) 7033–7044.

[24] L. Baussaron, C. Julcour-Lebigue, A.-M. Wilhelm, H. Delmas, C. Boyer, Wetting topology in trickle bed reactors, AIChE journal 53 (7) (2007) 1850–1860.

[25] L. Baussaron, C. Julcour-Lebigue, A.-M. Wilhelm, C. Boyer, H. Delmas, Partial wetting in trickle bed reactors: measurement techniques and global wetting efficiency, Industrial & engineering chemistry research 46 (25) (2007) 8397–8405.

[26] A. V. Sapre, D. H. Anderson, F. Krambeck, Heater probe technique to measure flow maldistribution in large scale trickle bed reactors, Chemical Engineering Science 45 (8) (1990) 2263–2268.

[27] N. A. Tsochatzidis, A. J. Karabelas, D. Giakoumakis, G. A. Huff, An investigation of liquid maldistribution in trickle beds, Chemical Engineering Science 57 (17) (2002) 3543–3555.

[28] P. R. Gunjal, V. V. Ranade, R. V. Chaudhari, Liquid distribution and RTD in trickle bed reactors: experiments and CFD simulations, The Canadian Journal of Chemical Engineering 81 (3-4) (2003) 821–830.

[29] P. G. Lutran, K. M. Ng, E. P. Delikat, Liquid distribution in trickle-beds. an experimental study using computer-assisted tomography, Industrial & Engineering Chemistry Research 30 (6) (1991) 1270–1280.

[30] B. Qi, O. Farid, S. Uribe, M. Al-Dahhan, Maldistribution and dynamic liquid holdup quantification of quadrilobe catalyst in a trickle bed reactor using gamma-ray computed tomography: Pseudo-3D modelling and empirical modelling using deep neural network, Chemical Engineering Research and Design 164 (2020) 195–208.

[31] C. Boyer, B. Fanget, Measurement of liquid flow distribution in trickle bed reactor of large diameter with a new gamma-ray tomographic system, Chemical Engineering Science 57 (7) (2002) 1079–1089.

[32] N. Reinecke, D. Mewes, Tomographic imaging of trickle-bed reactors, Chemical Engineering Science 51 (10) (1996) 2131–2138.

[33] M. Schubert, A. Khetan, M. J. Da Silva, H. Kryk, Spatially resolved inline measurement of liquid velocity in trickle bed reactors, Chemical Engineering Journal 158 (3) (2010) 623–632.

[34] L. F. Gladden, L. D. Anadon, C. P. Dunckley, M. D. Mantle, A. J. Sederman, Insights into gas–liquid–solid reactors obtained by magnetic resonance imaging, Chemical Engineering Science 62 (24) (2007) 6969–6977.

[35] N. L. Nguyen, V. Van Buren, A. Von Garnier, E. H. Hardy, R. Reimert, Application of Magnetic Resonance Imaging (MRI) for investigation of fluid dynamics in trickle bed reactors and of droplet separation kinetics in packed beds, Chemical Engineering Science 60 (22) (2005) 6289–6297.

[36] A. J. Sederman, L. F. Gladden, Magnetic resonance imaging as a quantitative probe of gas–liquid distribution and wetting efficiency in trickle-bed reactors, Chemical Engineering Science 56 (8) (2001) 2615–2628.

[37] A. J. Sederman, L. F. Gladden, Magnetic resonance visualisation of single- and two-phase flow in porous media, Magnetic resonance imaging 19 (3-4) (2001) 339–343.

[38] L. F. Gladden, M. H. M. Lim, M. D. Mantle, A. J. Sederman, E. H. Stitt, MRI visualisation of two-phase flow in structured supports and trickle-bed reactors, Catalysis Today 79 (2003) 203–210.

[39] M. Mantle, A. J. Sederman, L. F. Gladden, Single-and two-phase flow in fixed-bed reactors: MRI flow visualisation and lattice-boltzmann simulations, Chemical Engineering Science 56 (2) (2001) 523–529.

[40] M. H. Sankey, D. J. Holland, A. J. Sederman, L. F. Gladden, Magnetic resonance velocity imaging of liquid and gas two-phase flow in packed beds, Journal of Magnetic Resonance 196 (2) (2009) 142–148.

[41] N. P. Rice, Investigation of multiphase reactor hydrodynamics using magnetic resonance imaging, Ph.D. thesis, University of Cambridge (2019).

[42] M. H. M. Lim, A. J. Sederman, L. F. Gladden, E. H. Stitt, New insights to trickle and pulse flow hydrodynamics in trickle-bed reactors using MRI, Chemical Engineering Science 59 (22-23) (2004) 5403–5410.

[43] L. D. Anadon, A. J. Sederman, L. F. Gladden, Mechanism of the trickle-to-pulse flow transition in fixed-bed reactors, AIChE journal 52 (4) (2006) 1522–1532.

[44] A. Stadler, W. Schima, A. Ba-Ssalamah, J. Kettenbach, E. Eisenhuber, Artifacts in body MR imaging: their appearance and how to eliminate them, European radiology 17 (5) (2007) 1242–1255.

[45] W. S. Rasband, Imagej, u. s. national institutes of health, bethesda, maryland, usa, http://imagej.nih.gov/ij/ (1997-2018).

[46] I. The MathWorks, Matlab (version 9.6 (R2019a)).

[47] D.-J. Kroon, Read Medical Data 3D, Matlab Central File Exchange, `https://www.mathworks.com/matlabcentral/fileexchange/29344-read-medical-data-3d` (2022)).

[48] J. N. Kapur, P. K. Sahoo, A. K. Wong, A new method for gray-level picture thresholding using the entropy of the histogram, Computer Vision, Graphics, and Image Processing 29 (3) (1985) 273–285.

[49] D. Legland, I. Arganda-Carreras, P. Andrey, Morpholibj: integrated library and plugins for mathematical morphology with ImageJ, Bioinformatics 32 (22) (2016) 3532–3534.

[50] L. Xie, Spherical hough transform for 3D images(https://www.mathworks.com/matlabcentral/fileexchange/48219-spherical-hough-transform-for-3d-images) (Retrieved December 10, 2022).

[51] M. Markl, Velocity encoding and flow imaging, University Hospital Freiburg, Dept of Diagnostic Radiology (2005).

[52] Q.-S. Xiang, Temporal phase unwrapping for cine velocity imaging, Journal of Magnetic Resonance Imaging 5 (5) (1995) 529–534.

[53] N. J. Pelc, M. A. Bernstein, A. Shimakawa, G. H. Glover, Encoding strategies for three-direction phase-contrast mr imaging of flow, Journal of Magnetic Resonance Imaging 1 (4) (1991) 405–413.

[54] M. Kasim, Fast 2D phase unwrapping implementation in matlab, GitHub (2017).

[55] M. A. Herráez, D. R. Burton, M. J. Lalor, M. A. Gdeisat, Fast two-dimensional phase-unwrapping algorithm based on sorting by reliability following a noncontinuous path, Applied Optics 41 (35) (2002) 7437–7444.

[56] A. Fathiganjehlou, A. Eghbalmanesh, M. W. Baltussen, E. A. J. F. Peters, K. A. Buist, J. A. M. Kuipers, Pore network modelling of slender packed bed reactors, Chemical Engineering Science (2023) 118626.

[57] S. Das, N. G. Deen, J. A. M. Kuipers, A DNS study of flow and heat transfer through slender fixed-bed reactors randomly packed with spherical particles, Chemical Engineering Science 160 (2017) 1–19.

[58] H.-J. Choi, M. S. Kim, D. Ahn, S. Y. Yeo, S. Lee, Electrical percolation threshold of carbon black in a polymer matrix and its application to antistatic fibre, Scientific reports 9 (1) (2019) 6338.

[59] S. Alamri, A. I. Aguilar-Morales, A. F. Lasagni, Controlling the wettabil-
ity of polycarbonate substrates by producing hierarchical structures using
direct laser interference patterning, European Polymer Journal 99 (2018)
27–37.